

Model ingredients and peak mass production in heavy-ion collisions

Sukhjit Kaur¹ and Aman D. Sood^{2,*}

¹*House No. 465, Sector-1B, Nasruli, Mandi Gobindgarh-147301, Punjab, India and*

²*SUBATECH, Laboratoire de Physique Subatomique et des Technologies Associées,
Université de Nantes - IN2P3/CNRS - EMN*

4 rue Alfred Kastler, F-44072 Nantes, France.

(Dated: December 1, 2018)

We simulate the central reactions of $^{20}\text{Ne}+^{20}\text{Ne}$, $^{40}\text{Ar}+^{45}\text{Sc}$, $^{58}\text{Ni}+^{58}\text{Ni}$, $^{86}\text{Kr}+^{93}\text{Nb}$, $^{129}\text{Xe}+^{118}\text{Sn}$, $^{86}\text{Kr}+^{197}\text{Au}$, and $^{197}\text{Au}+^{197}\text{Au}$ at different incident energies for different equations of state, different binary cross sections and different widths of Gaussians. A rise-and-fall behavior of the multiplicity of intermediate mass fragments (IMFs) is observed. The system size dependence of peak center-of-mass energy $E_{c.m.}^{max}$ and peak IMF multiplicity $\langle N_{IMF} \rangle^{max}$ is also studied, where it is observed that $E_{c.m.}^{max}$ follows a linear behavior and $\langle N_{IMF} \rangle^{max}$ shows a power-law dependence. A comparison between two clusterization methods, the minimum spanning tree and the minimum spanning tree method with binding energy check (MSTB), is also made. We find that the MSTB method reduces the $\langle N_{IMF} \rangle^{max}$, especially in heavy systems. The power-law dependence is also observed for fragments of different sizes at $E_{c.m.}^{max}$ and the power-law parameter τ is found to be close to unity in all cases except A^{max} .

PACS numbers: 25.70.Pq, 25.70.-z

I. INTRODUCTION

At high excitation energies, the colliding nuclei may break into several small and intermediate size fragments and a large number of nucleons are also emitted [1–3]. The emission of intermediate mass fragments (IMFs) in nuclear collisions was studied for more than a decade during which several experimental groups have carried out a complete study of fragment formation with 4π detectors [4–10]. These studies revealed that the fragments formed in heavy-ion collisions depend crucially on the bombarding energy and impact parameter of the reaction [1–5]. Therefore, these experimental studies of fragmentation offer a unique opportunity to explore the mechanism behind the formation of the fragments. Moreover, one can also pin down the role of dynamics in fragment formation and its time scale.

Recently, there has been increasing interest in the effects of reaction dynamics on the production of IMFs and light charged particles (LCPs, $Z = 1$ or 2). Sisan *et al.* [6] studied the emission of IMFs from central collisions of nearly symmetric systems using a 4π -array set up, where they found that the multiplicity of IMFs shows a rise and fall with increase in the beam energy. They observed that $E_{c.m.}^{max}$ (the energy at which the maximum production of IMFs occurs) increases linearly with the system mass, whereas a power-law ($\propto A^\tau$) dependence was reported for peak multiplicity of IMFs with power factor $\tau = 0.7$. Peaslee *et al.* [7], however, studied the asymmetric system $^{84}\text{Kr}+^{197}\text{Au}$ in the incident energy range from 35 to 400 MeV/nucleon and obtained an energy dependence of multifragmentation. Their findings

revealed that fragment production increases up to 100 MeV/nucleon and then decreases with increase in incident energy. De Souza *et al.* [8] studied the central collisions of $^{36}\text{Ar}+^{197}\text{Au}$ from 35 to 120 MeV/nucleon and observed that IMF multiplicity shows a steady increase with increase in the incident energy. The IMF multiplicity decreases, however, when one moves from central to peripheral collisions. However, Tsang *et al.* [5], in their investigation of $^{197}\text{Au}+^{197}\text{Au}$ collisions at $E/A = 100, 250, \text{ and } 400$ MeV, found the occurrence of peak multiplicity at lower energies for central collisions whereas it is shifted to higher energies for peripheral collisions. Stone *et al.* [9] used a nearly symmetric system of $^{86}\text{Kr}+^{93}\text{Nb}$ from 35 to 95 MeV/nucleon to obtain IMF multiplicity distribution as a function of beam energy by selecting central events. Ogilvie *et al.* [10] also studied the multifragment decays of Au projectiles after collisions with C, Al, and Cu targets at the bombarding energy of 600 MeV/nucleon using the ALADIN forward spectrometer at GSI, Darmstadt, with the beam accelerated by Schwerionensynchrotron (SIS). They found that, with increasing violence of collision, the mean multiplicity of IMFs originating from the projectile first increases to a maximum and then decreases again. As mentioned earlier, Sisan *et al.* [6] reported that the peak multiplicity of IMFs as well as peak center-of-mass energy scale with the size of the system. In a recent communication, Vermani and Puri [11] succeeded partially in explaining the above-mentioned behavior by using the quantum molecular dynamics (QMD) approach. Here we plan to extend the above study by incorporating various model ingredients such as equation of state, nucleon-nucleon (nn) cross section, and Gaussian width. The role of different clusterization algorithms is also explored. We attempt to find out whether these ingredients have sizable effects.

*Electronic address: amandsood@gmail.com

II. THE FORMALISM

A. Quantum molecular dynamics model

We describe the time evolution of a heavy-ion reaction within the framework of a QMD model [1–3, 12], which is based on a molecular dynamics picture. Here each nucleon is represented by a coherent state of the form

$$\phi_\alpha(x_1, t) = \left(\frac{2}{L\pi}\right)^{\frac{3}{4}} e^{-(x_1-x_\alpha(t))^2} e^{ip_\alpha(x_1-x_\alpha)} e^{-\frac{ip_\alpha^2 t}{2m}}. \quad (1)$$

Thus, the wave function has two time-dependent parameters, x_α and p_α . The total n -body wave function is assumed to be a direct product of coherent states:

$$\phi = \phi_\alpha(x_1, x_\alpha, p_\alpha, t) \phi_\beta(x_2, x_\beta, p_\beta, t) \dots, \quad (2)$$

where antisymmetrization is neglected. One should, however, keep in the mind that the Pauli principle, which is very important at low incident energies, was taken into account. The initial values of the parameters are chosen in a way that the ensemble ($A_T + A_P$) nucleons give a proper density distribution as well as a proper momentum distribution of the projectile and target nuclei. The time evolution of the system is calculated using the generalized variational principle. We start out from the action

$$S = \int_{t_1}^{t_2} \mathcal{L}[\phi, \phi^*] d\tau, \quad (3)$$

with the Lagrange functional

$$\mathcal{L} = \left(\phi \left| i\hbar \frac{d}{dt} - H \right| \phi \right), \quad (4)$$

where the total time derivative includes the derivatives with respect to the parameters. The time evolution is obtained by the requirement that the action is stationary under the allowed variation of the wave function

$$\delta S = \delta \int_{t_1}^{t_2} \mathcal{L}[\phi, \phi^*] dt = 0. \quad (5)$$

If the true solution of the Schrödinger equation is contained in the restricted set of wave function $\phi_\alpha(x_1, x_\alpha, p_\alpha)$, this variation of the action gives the exact solution of the Schrödinger equation. If the parameter space is too restricted, we obtain that wave function in the restricted parameter space, which comes close to the solution of the Schrödinger equation. Performing the variation with the test wave function (2), we obtain for each parameter λ an Euler-Lagrange equation:

$$\frac{d}{dt} \frac{\partial \mathcal{L}}{\partial \dot{\lambda}} - \frac{\partial \mathcal{L}}{\partial \lambda} = 0. \quad (6)$$

For each coherent state and a Hamiltonian of the form,

$H = \sum_\alpha \left[T_\alpha + \frac{1}{2} \sum_{\alpha\beta} V_{\alpha\beta} \right]$, the Lagrangian and the Euler-Lagrange function can be easily calculated [12]:

$$\mathcal{L} = \sum_\alpha \dot{\mathbf{x}}_\alpha \mathbf{p}_\alpha - \sum_\beta \langle V_{\alpha\beta} \rangle - \frac{3}{2Lm}, \quad (7)$$

$$\dot{\mathbf{x}}_\alpha = \frac{\mathbf{p}_\alpha}{m} + \nabla_{p_\alpha} \sum_\beta \langle V_{\alpha\beta} \rangle, \quad (8)$$

$$\dot{\mathbf{p}}_\alpha = -\nabla_{\mathbf{x}_\alpha} \sum_\beta \langle V_{\alpha\beta} \rangle. \quad (9)$$

Thus, the variational approach has reduced the n -body Schrödinger equation to a set of $6n$ different equations for the parameters that can be solved numerically. If one inspects the formalism carefully, one finds that the interaction potential, which is actually the Brückner G -matrix, can be divided into two parts: (i) a real part and (ii) an imaginary part. The real part of the potential acts like a potential, whereas the imaginary part is proportional to the cross section.

In the present model, the interaction potential comprises of the following terms:

$$V_{\alpha\beta} = V_{loc}^2 + V_{loc}^3 + V_{Coul} + V_{Yuk} + V_{MDI}, \quad (10)$$

where V_{loc} is the Skyrme force and V_{Coul} , V_{Yuk} and V_{MDI} define, respectively, the Coulomb, Yukawa and momentum dependent potentials. The Yukawa term separates the surface which also plays a role in low-energy processes like fusion and cluster radioactivity [13, 14]. The expectation value of these potentials is calculated as

$$V_{loc}^2 = \int f_\alpha(\mathbf{p}_\alpha, \mathbf{r}_\alpha, t) f_\beta(\mathbf{p}_\beta, \mathbf{r}_\beta, t) V_I^{(2)}(\mathbf{r}_\alpha, \mathbf{r}_\beta) \times d^3\mathbf{r}_\alpha d^3\mathbf{r}_\beta d^3\mathbf{p}_\alpha d^3\mathbf{p}_\beta, \quad (11)$$

$$V_{loc}^3 = \int f_\alpha(\mathbf{p}_\alpha, \mathbf{r}_\alpha, t) f_\beta(\mathbf{p}_\beta, \mathbf{r}_\beta, t) f_\gamma(\mathbf{p}_\gamma, \mathbf{r}_\gamma, t) \times V_I^{(3)}(\mathbf{r}_\alpha, \mathbf{r}_\beta, \mathbf{r}_\gamma) d^3\mathbf{r}_\alpha d^3\mathbf{r}_\beta d^3\mathbf{r}_\gamma \times d^3\mathbf{p}_\alpha d^3\mathbf{p}_\beta d^3\mathbf{p}_\gamma. \quad (12)$$

where $f_\alpha(\mathbf{p}_\alpha, \mathbf{r}_\alpha, t)$ is the Wigner density which corresponds to the wave functions [Eq. 2]. If we deal with the local Skyrme force only, we get

$$V^{Skyrme} = \sum_{\alpha=1}^{A_T+A_P} \left[\frac{A}{2} \sum_{\beta=1} \left(\frac{\tilde{\rho}_{\alpha\beta}}{\rho_0} \right) + \frac{B}{C+1} \sum_{\beta \neq \alpha} \left(\frac{\tilde{\rho}_{\alpha\beta}}{\rho_0} \right)^C \right]. \quad (13)$$

Here A , B and C are the Skyrme parameters which are defined according to the ground-state properties of a nucleus. Different values of C lead to different equations of state. A larger value of C ($= 380$ MeV) is often dubbed

a stiff equation of state. The finite range Yukawa (V_{Yuk}) potential and effective Coulomb potential (V_{Coul}) read as

$$V_{Yuk} = \sum_{j,i \neq j} t_3 \frac{\exp\{-|\mathbf{r}_i - \mathbf{r}_j|\}/\mu}{|\mathbf{r}_i - \mathbf{r}_j|/\mu}, \quad (14)$$

$$V_{Coul} = \sum_{j,i \neq j} \frac{Z_{eff}^2 e^2}{|\mathbf{r}_i - \mathbf{r}_j|}. \quad (15)$$

The Yukawa interaction (with $t_3 = -6.66$ MeV and $\mu = 1.5$ fm) is essential for the surface effects. The momentum-dependent interactions (MDI) are obtained by parameterizing the momentum dependence of the real part of the optical potential. The final form of the potential reads as follows [12]:

$$U^{MDI} \approx t_4 \ln^2[t_5(\mathbf{p}_1 - \mathbf{p}_2)^2 + 1] \delta(\mathbf{r}_1 - \mathbf{r}_2). \quad (16)$$

where $t_4 = 1.57$ MeV and $t_5 = 5 \times 10^{-4}$ MeV $^{-2}$. A parameterized form of the local plus MDI potential is given by

$$U = \alpha \left(\frac{\rho}{\rho_0}\right) + \beta \left(\frac{\rho}{\rho_0}\right) + \delta \ln^2[\epsilon(\rho/\rho_0)^{2/3} + 1] \rho/\rho_0. \quad (17)$$

The parameters α , β , γ , δ and ϵ are listed in Ref. [12]. The momentum-dependent part of the interaction acts strongly in the cases where the system is mildly excited [15, 16]. In this case, the MDI is reported to generate a lot more fragments compared to the static equation of state. For a detailed discussion of the different equations of state and MDI, the reader is referred to Refs. [4, 15, 16]. The relativistic effect does not play a role in the low incident energy of present interest.

The phase space of the nucleons is stored at several time steps. The QMD model does not give any information about the fragments observed at the final stage of the reaction. To construct fragments from the present phase space, one needs the clusterization algorithms. We concentrate here on the minimum spanning tree (MST) method and the minimum spanning tree method with binding energy check (MSTB) only.

B. Different clusterization methods

1. Minimum spanning tree method

The widely used clusterization algorithm is the MST method [17]. In the MST method, two nucleons are allowed to share the same fragment if their centroids are closer than a distance r_{min} ,

$$|\mathbf{r}_i - \mathbf{r}_j| \leq r_{min}, \quad (18)$$

where \mathbf{r}_i and \mathbf{r}_j are the spatial positions of both nucleons. The value of r_{min} can vary between 2 and 4 fm. This method cannot address the question of time scale. This method gives a big fragment at high density, which splits into several light and medium mass fragments after several hundred fm/c. This procedure gives same fragment pattern for times later than 200 fm/c, but cannot be used for earlier times.

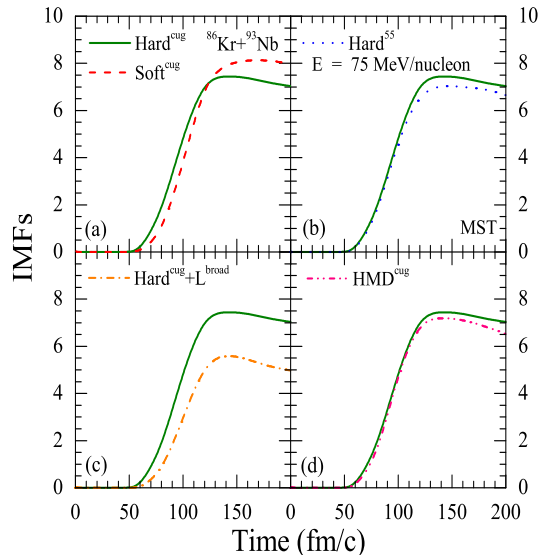


FIG. 1: (Color online) The time evolution of IMFs ($5 \leq A \leq 44$) for the reaction of $^{86}\text{Kr}+^{93}\text{Nb}$ at incident energy of 75 MeV/nucleon for different model ingredients.

2. Minimum spanning tree method with binding energy check

This is an improved version of the normal MST method. First, the simulated phase space is analyzed with the MST method and pre-clusters are sorted out. Each of the pre-clusters is then subjected to a binding energy check [11, 17]:

$$\zeta_i = \frac{1}{N^f} \sum_{i=1}^{N^f} \left[\frac{(\mathbf{p}_i - P_{N^f}^{c.m.})^2}{2m_i} + \frac{1}{2} \sum_{j \neq i}^{N^f} V_{ij}(\mathbf{r}_i, \mathbf{r}_j) \right] < E_{bind}. \quad (19)$$

We take $E_{bind} = -4.0$ MeV if $N^f \geq 3$ and $E_{bind} = 0.0$ otherwise. Here N^f is the number of nucleons in a fragment and $P_{N^f}^{c.m.}$ is the center-of-mass momentum of the fragment. This is known as the minimum spanning tree method with Binding energy check (MSTB) [11, 17]. The fragments formed with the MSTB are reliable and stable at early stages of the reactions.

III. RESULTS AND DISCUSSION

We simulated the central reactions of $^{20}\text{Ne}+^{20}\text{Ne}$ ($E_{lab} = 10-55$ MeV/nucleon), $^{40}\text{Ar}+^{45}\text{Sc}$ ($E_{lab} = 35-115$ MeV/nucleon), $^{58}\text{Ni}+^{58}\text{Ni}$ ($E_{lab} = 35-105$ MeV/nucleon), $^{86}\text{Kr}+^{93}\text{Nb}$ ($E_{lab} = 35-95$ MeV/nucleon), $^{129}\text{Xe}+^{118}\text{Sn}$ ($E_{lab} = 45-140$ MeV/nucleon), $^{86}\text{Kr}+^{197}\text{Au}$ ($E_{lab} = 35-400$ MeV/nucleon) and $^{197}\text{Au}+^{197}\text{Au}$ ($E_{lab} = 70-130$ MeV/nucleon). The energies are guided by experiments [5–7]. For the present study, we use hard (labeled Hard), soft (Soft), hard with MDI (HMD), and soft with

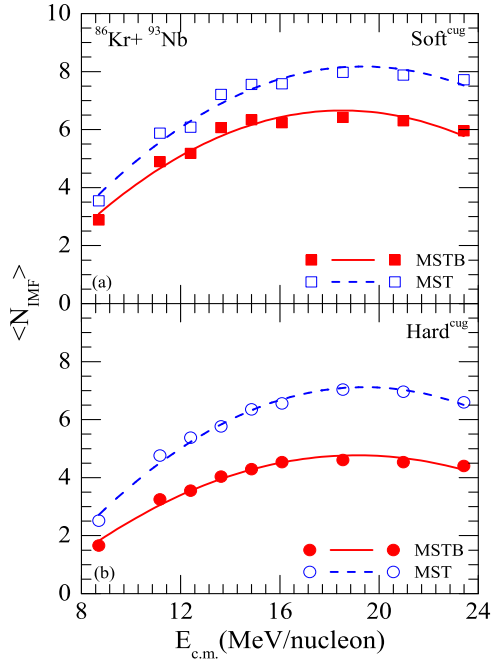


FIG. 2: (Color online) The mean IMF multiplicity, $\langle N_{IMF} \rangle$, as a function of incident energy in center-of-mass frame, $E_{c.m.}$, for the reaction $^{86}\text{Kr} + ^{93}\text{Nb}$. Solid (dashed) curves show the quadratic fits to the model calculations for MSTB (MST) to estimate the peak center-of-mass energy at which the maximal IMF emission occurs.

MDI (SMD) equations of state. We also use the standard energy-dependent Cugnon cross section (σ_{nn}^{free}) [16] and constant isotropic cross section of 55 mb strength in addition to two different widths of Gaussian $L = 1.08$ and 2.16 fm^2 (L^{broad}). The superscripts represent cross section. The phase space is clustered using the clusterization methods described previously. The reactions are followed until 200 fm/c but the conclusions do not change when the reaction is complete, employing the validity of both algorithms.

In fig. 1, we display the time evolution of IMFs for the reaction $^{86}\text{Kr} + ^{93}\text{Nb}$ at incident energy of 75 MeV/nucleon employing the MST method. In fig. 1(a), we display the model calculations using Hard^{Cug} (solid line) and Soft^{Cug} (dashed line). From fig. 1(a), we see that the number of IMFs is larger in case of Soft compared to that of Hard. This is because of the fact that soft matter is easily compressed, resulting in greater achieved density, which in turn leads to the large number of IMFs compared to that in the Hard. It is worth mentioning here that the effect could be opposite at higher energies, because at higher energies the IMFs may further break into LCPs and free nucleons. In fig. 1(b), we display the results for Hard^{Cug} and Hard^{55} (dotted line). As evident from the fig. 1(b), the number of IMFs is nearly same for both types of cross sections. This may

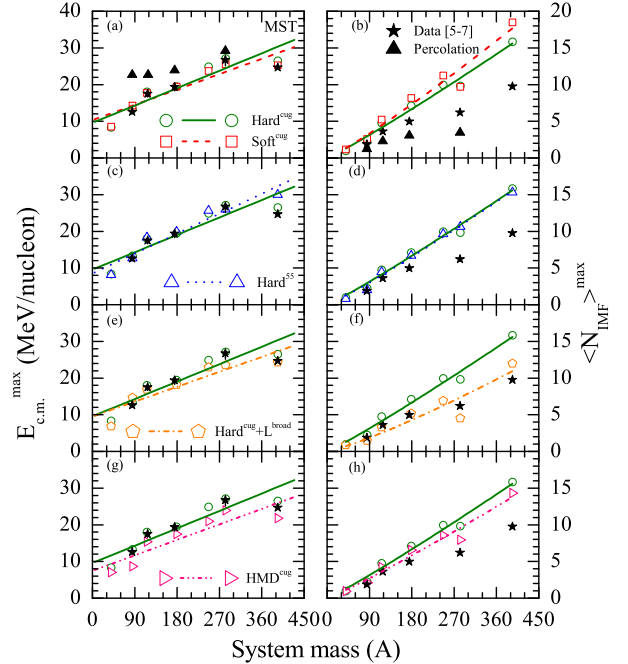


FIG. 3: (Color online) The $E_{c.m.}^{max}$ (left) and $\langle N_{IMF} \rangle^{max}$ (right) as a function of composite mass of the system (A). The different lines in left (right) panels represent the linear fits (power-law fits). Comparison of model calculations is made with experimental data [5–7] (solid stars). The percolation calculations [6] (solid triangles) are also shown in figure.

be because, for the central collisions, since the excitation energy is already high, different cross sections have a negligible role to play. In fig. 1(c), we display the results for the Hard case along with two different widths of the Gaussian, that is, L and L^{broad} (dash-dotted line). We find that the width of Gaussian has a considerable impact on fragmentation. As we change the Gaussian width (L) from 4.33 to 8.66 fm^2 , the multiplicity of IMFs is reduced by $\approx 30\%$. Interestingly, the kaon yield also gets reduced by the same amount [18]. Owing to its large interaction range, an extended wave packet (i.e. L^{broad}) connects a large number of nucleons in a fragment, as a result, it generates heavier fragments compared to what is obtained with a smaller width. It is worth mentioning here that the width of the Gaussian has a considerable effect on the collective flow [18, 19] as well as on pion production [18, 20]. In fig. 1(d), we display the results using Hard and HMD (dash-dot-dotted line). Again the number of IMFs are nearly same for both equations of state (EOS). This is expected because the effect of MDI is small at these energies. However, the scenario is completely different at high energies; at high energies, owing to the repulsive nature of MDI, there is a large destruction of initial correlations and the additional momentum dependence further destroys the correlations reducing further

the multiplicity of IMFs. This leads to the emission of lots of nucleons and LCPs [21].

In fig. 2, we display the average multiplicity of IMFs, $\langle N_{IMF} \rangle$, as a function of incident energy in the center-of-mass frame ($E_{c.m.}$) for the $^{86}\text{Kr}+^{93}\text{Nb}$ reaction employing the MST (open symbols) and the MSTB (solid symbols) methods. Figures. 2(a) and 2(b) are for Soft^{Cug} and Hard^{Cug} , respectively. Lines represent the quadratic fit to the model calculations. In both cases, the number of IMFs first increases with incident energy, attains a maximum, and then decreases, in agreement with previous studies [5–7, 10, 11]. Clearly, $\langle N_{IMF} \rangle$ is greater for the MST method than for MSTB, because in the case of the MSTB, along with spatial correlations, an additional check for binding energy is also used; therefore, it filters out the loosely bound fragments which decay later. Hence, the fragments obtained with THE MSTB are properly bound. A similar trend is obtained for all other reactions as well as different model ingredients used in the present study but is less pronounced in lighter systems like $^{20}\text{Ne}+^{20}\text{Ne}$ and $^{40}\text{Ar}+^{45}\text{Sc}$ as compared to heavier systems. However, for the Gaussian width L^{broad} , the value of $\langle N_{IMF} \rangle$ is nearly zero in this incident energy range using THE MSTB (not shown here). This is because an extended wave packet (i.e. L^{broad}) connects a large number of nucleons in a fragment; as a result, it generates heavier fragments and the additional binding energy check further excludes the unbound fragments.

In fig. 3, we display the peak center-of-mass energy $E_{c.m.}^{max}$ (left panels) and peak multiplicity of IMFs $\langle N_{IMF} \rangle^{max}$ (right panels) as a function of the combined mass of the system employing the MST method. In the left panels, lines represent linear fitting proportional to mA and in the right panels, lines represent power-law fitting proportional to A^τ . The multiplicity of IMFs, in the case of $^{20}\text{Ne}+^{20}\text{Ne}$ and $^{40}\text{Ar}+^{45}\text{Sc}$, is obtained by excluding the largest and second largest fragment, respectively, to get the accurate information about the system size dependence. $\langle N_{IMF} \rangle^{max}$ and corresponding $E_{c.m.}^{max}$ are obtained by making a quadratic fit to the model calculations for $\langle N_{IMF} \rangle$ as a function of ($E_{c.m.}$). From the left panels, we find that the mass dependence of $E_{c.m.}^{max}$ is insensitive to different EOS (fig. 3a), nn cross section (fig. 3b), as well as the width of the Gaussian [fig. 3c]. It is slightly sensitive to MDI because, for heavy systems, the value of $E_{c.m.}^{max}$ is greater, as a result of which is that the effect of MDI becomes non-negligible and creates the $\langle N_{IMF} \rangle^{max}$ at smaller energies. From the right panels where we display the mass dependence of $\langle N_{IMF} \rangle^{max}$, we find that the peak multiplicity is insensitive to cross section (fig. 3d) and MDI (fig. 3h) (for explanation see discussion of fig. 1). It is slightly sensitive to the EOS (fig. 3b) but highly sensitive to the Gaussian width (fig. 3f). On increasing the width of the Gaussian, $\langle N_{IMF} \rangle^{max}$ reduces to a large extent. As discussed earlier, an extended wave packet (i.e. L^{broad}) will connect a large number of nucleons in a fragment; as a result, it generates heavier fragments compared to what one obtains with smaller width.

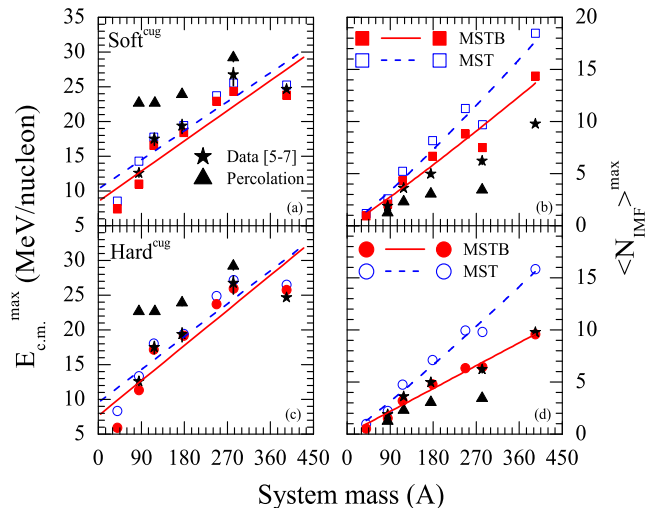


FIG. 4: (Color online) The $E_{c.m.}^{max}$ (left panels) and $\langle N_{IMF} \rangle^{max}$ (right panels) as a function of composite mass of the system (A) using Soft^{Cug} (upper panels) and Hard^{Cug} (lower panels) employing THE MSTB and THE MST methods. Lines have same meaning as in fig. 3. Comparison of model calculations is made with experimental data [5–7] (solid stars).

From fig. 3, we see that $E_{c.m.}^{max}$ shows linear dependence ($\propto mA$) whereas $\langle N_{IMF} \rangle^{max}$ follows power-law behavior ($\propto A^\tau$) with τ nearly equal to unity.

In fig. 3, the model calculations are also compared with experimental data [5–7]. It is clear from fig. 3 that model calculations for $E_{c.m.}^{max}$ agree with experimental data [5–7] whereas in the case of $\langle N_{IMF} \rangle^{max}$, as the system mass increases, the difference between model calculations and experimental results continues to increase. This behavior is consistent for all the different choices of model ingredients. This may be because the fragments obtained with the MST method are not reliable because this method makes sense only when matter is diluted and well separated. This is true only in the case of high beam energy and in central collisions. Therefore, we have to look for other methods of clusterization. As mentioned earlier, the fragments obtained with the MSTB are properly bound and reliable. So, as a next step, we check the system size dependence of $E_{c.m.}^{max}$ and $\langle N_{IMF} \rangle^{max}$ by using the MSTB for clusterization.

In fig. 4, we display the $E_{c.m.}^{max}$ (left panels) and $\langle N_{IMF} \rangle^{max}$ (right panels) for Soft^{Cug} (upper panels) and Hard^{Cug} (bottom panels) as a function of the combined mass of the system. Solid (open) symbols represent the MSTB (MST method). From the left-hand panels, we find that $E_{c.m.}^{max}$ remains insensitive to the choice of clusterization method. The same is true for $\langle N_{IMF} \rangle^{max}$ (right-hand panels) but in low-mass region. As the system mass increases, $\langle N_{IMF} \rangle^{max}$ becomes more and more sensitive to the method of clusterization. The MSTB excludes the loosely bound fragments, thus reducing the peak IMF multiplicity. The effect is uniform both for the

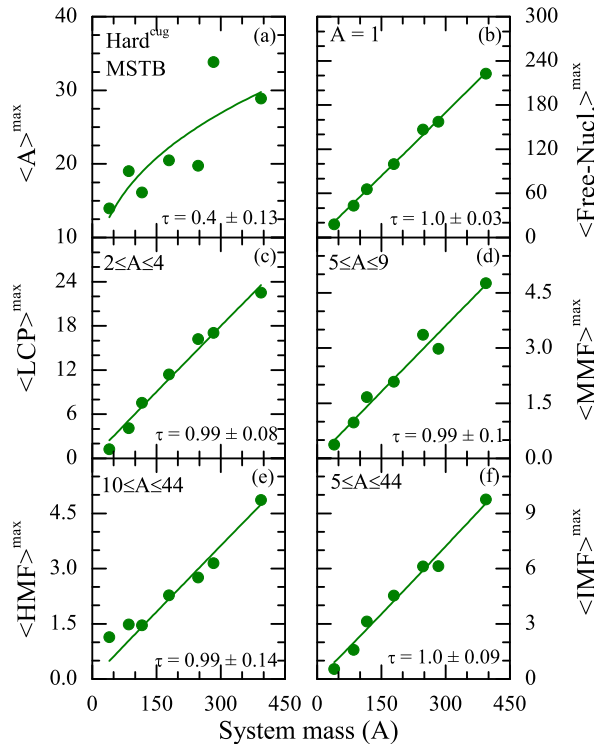


FIG. 5: (Color online) The largest fragment and multiplicities of free-nucleons, LCPs, MMFs, HMFs, and IMFs as a function of composite mass of the colliding nuclei (A) for different reactions at their respective $E_{c.m.}^{max}$ (solid circles). Lines represent the power-law fits ($\propto A^\tau$).

EOS and for different cross sections (not shown here).

In fig. 5, we display peak multiplicity (obtained by employing the MSTB) as a function of composite mass of the system for various fragments consisting of the largest fragment (A^{max}) (fig. 5a), free-nucleons ($1 \leq A \leq 1$) (fig. 5b), light charged particles (LCPs) ($2 \leq A \leq 4$) (fig. 5c), medium mass fragments (MMFs) ($5 \leq A \leq 9$) (fig. 5d), heavy mass fragments (HMFs) ($10 \leq A \leq 44$) (fig. 5e) and intermediate mass fragments (IMFs) ($5 \leq A \leq 44$) (fig. 5f) for Hard^{Cug}. Lines represent the power-law fitting proportional to A^τ . Interestingly, the peak multiplicities of different fragments follow a power-law ($\propto A^\tau$). The power-law factor τ is almost unity in all cases except A^{max} for which there is no clear system size dependence. The system size dependence of various fragments was also predicted by Dhawan and Puri [22]. Their calculations at the energy of vanishing flow (i.e., the energy at which the transverse flow vanishes) clearly suggested the existence of a power-law system mass dependence for various fragment multiplicities.

To check the stability of fragments, we display in fig. 6, the binding energy per nucleon as a function of

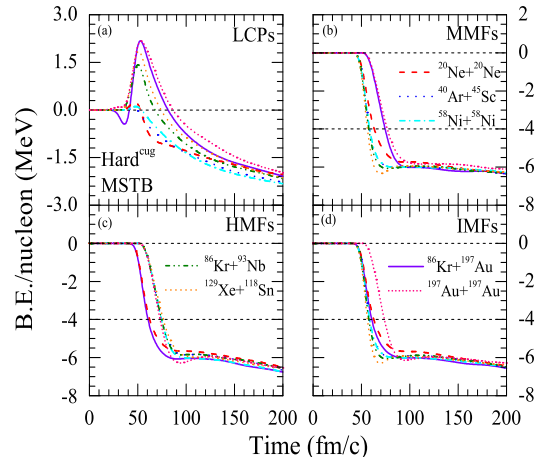


FIG. 6: (Color online) The time evolution of binding energy per nucleon for LCPs, MMFs, HMFs, and IMFs. Here reactions of $^{20}\text{Ne}+^{20}\text{Ne}$, $^{40}\text{Ar}+^{45}\text{Sc}$, $^{58}\text{Ni}+^{58}\text{Ni}$, $^{86}\text{Kr}+^{93}\text{Nb}$, $^{129}\text{Xe}+^{118}\text{Sn}$, $^{86}\text{Kr}+^{197}\text{Au}$, and $^{197}\text{Au}+^{197}\text{Au}$ are simulated for central geometry at their corresponding $E_{c.m.}^{max}$.

time for LCPs, MMFs, HMFs, and IMFs. The reactions of $^{20}\text{Ne}+^{20}\text{Ne}$, $^{40}\text{Ar}+^{45}\text{Sc}$, $^{58}\text{Ni}+^{58}\text{Ni}$, $^{86}\text{Kr}+^{93}\text{Nb}$, $^{129}\text{Xe}+^{118}\text{Sn}$, $^{86}\text{Kr}+^{197}\text{Au}$ and $^{197}\text{Au}+^{197}\text{Au}$ are simulated at laboratory energies corresponding to their $E_{c.m.}^{max}$ values, which are approximately 24, 46, 69, 78, 96, 124, and 105 MeV/nucleon, respectively. We find that, even at 200 fm/c, small fragments are still not cold and take a very long time to cool down, whereas the heavy fragments are properly bound, having binding energy per nucleon around -5 to -7 MeV.

IV. SUMMARY

We simulated the central reactions of nearly symmetric, and asymmetric systems over the entire periodic table at different incident energies for different EOS, nn cross sections, and different widths of Gaussians. We observed that the multiplicity of IMFs ($3 \leq Z \leq 20$) shows a rise and fall with increase in beam energy in the center-of-mass frame, as already predicted experimentally and theoretically. We also studied the system size dependence of peak center-of-mass energy $E_{c.m.}^{max}$ and peak IMF multiplicity $\langle N_{IMF} \rangle^{max}$. It was observed that $E_{c.m.}^{max}$ increases linearly with system mass whereas a power-law ($\propto A^\tau$) dependence was observed for $\langle N_{IMF} \rangle^{max}$ with $\tau \sim 1.0$. We compared the system size dependence of $E_{c.m.}^{max}$ and $\langle N_{IMF} \rangle^{max}$ for MST and MSTB methods and found that MSTB reduces the $\langle N_{IMF} \rangle^{max}$ especially in heavy systems because loosely bound fragments get excluded in MSTB. The power-law dependence is also observed for fragments of different sizes at the energy for which the

production of IMFs is a maximum and the power-law parameter τ is found to be close to unity in all cases except A^{max} . The stability of fragments is also checked through binding energy per nucleon. We observed that, at 200 fm/c, small fragments are still not cold and they take a very long time to cool down, whereas the heavy fragments are properly bound.

V. ACKNOWLEDGEMENTS

The work is supported by Indo-French project no. 4104-1.

-
- [1] R. K. Puri, C. Hartnack, and J. Aichelin, Phys. Rev. C **54**, R28 (1996); R. K. Puri and J. Aichelin, J. Comput. Phys. **162**, 245 (2000); Y. K. Vermani and R. K. Puri, Europhys. Lett. **85**, 62001 (2009); Y. K. Vermani, J. K. Dhawan, S. Goyal, R. K. Puri and J. Aichelin, J. Phys. G: Nucl. Part. Phys. **37**, 015105 (2010); S. Kumar, S. Kumar, and R. K. Puri, Phys. Rev. C **78**, 064602 (2008).
- [2] S. Kumar, M. K. Sharma, R. K. Puri, K. P. Singh, and I. M. Govil, Phys. Rev. C **58**, 3494 (1998); E. Lehmann *et al.*, Z. Phys. A **355**, 55 (1996); A. D. Sood and R. K. Puri, Phys. Rev. C **79**, 064618 (2009); A. D. Sood and R. K. Puri, Phys. Rev. C **70**, 034611 (2004); S. Kumar, S. Kumar, and R. K. Puri, Phys. Rev. C **81**, 014611 (2010); S. Kumar, S. Kumar, and R. K. Puri, Phys. Rev. C **81**, 014601 (2010); E. Lehmann *et al.*, Prog. Part. Nucl. Phys. **30**, 219 (1993); E. Lehmann, R. K. Puri, A. Faessler, G. Batko, and S. W. Huang, Phys. Rev. C **51**, 2113 (1995).
- [3] J. Singh, S. Kumar, and R. K. Puri, Phys. Rev. C **62**, 044617 (2000); G. Batko *et al.*, J. Phys. G: Nucl. Part. Phys. **20**, 461 (1994); S. W. Huang *et al.*, Prog. Part. Nucl. Phys. **30**, 105 (1993); R. K. Puri *et al.*, Nucl. Phys. A **575**, 733 (1994); C. Fuchs *et al.*, J. Phys. G: Nucl. Part. Phys. **22**, 131 (1996).
- [4] M. Begemann-Blaich *et al.*, Phys. Rev. C **48**, 610 (1993); D. R. Bowman *et al.*, Phys. Rev. Lett. **67**, 1527 (1991); A. Schuttauf *et al.*, Nucl. Phys. A **607**, 457 (1996); W. Reisdorf *et al.*, Nucl. Phys. A **612**, 493 (1997).
- [5] M. B. Tsang *et al.*, Phys. Rev. Lett. **71**, 1502 (1993).
- [6] D. Sisan *et al.*, Phys. Rev. C **63**, 027602 (2001).
- [7] G. F. Peaslee *et al.*, Phys. Rev. C **49**, R2271 (1994).
- [8] R. T. de Souza *et al.*, Phys. Lett. B **268**, 6 (1991).
- [9] N. T. B. Stone *et al.*, Phys. Rev. Lett. **78**, 2084 (1997).
- [10] C. A. Ogilvie *et al.*, Phys. Rev. Lett. **67**, 1214 (1991).
- [11] Y. K. Vermani and R. K. Puri, J. Phys. G: Nucl. Part. Phys. **36**, 105103 (2009).
- [12] J. Aichelin, Phys. Rep. **202**, 233 (1991).
- [13] R. K. Puri and R. K. Gupta, Phys. Rev. C **45**, 1837 (1992); R. K. Puri, M. K. Sharma, and R. K. Gupta, Eur. Phys. J A **3**, 277 (1998); R. K. Puri, P. Chattopadhyay, and R. K. Gupta, Phys. Rev. C **43**, 315 (1991); R. Arora, R. K. Puri, and R. K. Gupta, Eur. Phys. J A **8**, 103 (2000); I. Dutt and R. K. Puri, Phys. Rev. C **81**, 047601 (2010); *ibid* **81**, 044615 (2010); *ibid* **81**, 064609 (2010); *ibid* **81**, 064608 (2010); R. K. Puri and N. K. Dhiman, Eur. Phys. J A **23**, 429 (2005).
- [14] S. S. Malik *et al.*, Pram. J. Phys. **32**, 419 (1989); R. K. Puri, S. S. Malik, and R. K. Gupta, Europhys. Lett. **9**, 767 (1989); R. K. Puri and R. K. Gupta, J. Phys. G: Nucl. Part. Phys. **18**, 903 (1992); R. K. Gupta *et al.*, J. Phys. G: Nucl. Part. Phys. **26**, L23 (2000).
- [15] S. Kumar, and R. K. Puri, Phys. Rev. C **60**, 054607 (1999).
- [16] S. Kumar, R. K. Puri, and J. Aichelin, Phys. Rev. C **58**, 1618 (1998).
- [17] J. Singh and R. K. Puri, J. Phys. G: Nucl. Part. Phys. **27**, 2091 (2001); S. Kumar, and R. K. Puri, Phys. Rev. C **58**, 2858 (1998).
- [18] C. Hartnack *et al.*, Eur. Phys. J A **1**, 151 (1998).
- [19] S. Gautam *et al.*, J. Phys. G: Nucl. Part. Phys. **37**, 085102 (2010); S. Gautam and A. D. Sood, Phys. Rev. C **82**, 014604 (2010); A. D. Sood and R. K. Puri, Phys. Rev. C **69**, 054612 (2004); *ibid* **73**, 067602 (2006); *ibid* Eur. Phys. J. A **30**, 571 (2006).
- [20] C. Hartnack *et al.*, Nucl. Phys. A **580**, 643 (1994).
- [21] Y. K. Vermani, S. Goyal, and R. K. Puri, Phys. Rev. C **79**, 064613 (2009).
- [22] J. K. Dhawan and R. K. Puri, Phys. Rev. C **74**, 054610 (2006).